Conformational Control as a Design Strategy to Tune the Redox Behavior of Benzotriazole Negolytes for Non-Aqueous Flow Batteries

Palani Sabhapathy,[a] Uddalak Sengupta,[b] Miguel Munoz,[a] Eda Cagli,[a] Matthew T. Figgins,[b] Jesse Wainright,[a] David C. Powers,[b,*] and Burcu Gurkan[a,*]

[a] Department of Chemical and Biomolecular Engineering, Case Western Reserve University, Cleveland, Ohio 44106, United States

[b] Department of Chemistry, Texas A&M University, College Station, Texas 77843, United States

* powers@chem.tamu.edu; beg23@case.edu

ABSTRACT

Here, we present a molecular engineering strategy to tune the reduction potentials of benzotriazole derivatives as high-energy-density negolytes in non-aqueous redox flow batteries. Within non-aqueous electrolytes, these derivatives, notably 2-(*o*-tolyl)-2*H*-benzo[*d*][1,2,3]triazole (**1**), demonstrate a theoretical capacity of up to 93.8 Ah L^{-1} and a reduction potential of –2.35 V *vs.* ferrocene/ferrocenium (Fc/Fc^{+}). Introducing dimethyl substitution (*i.e.*, 2-(2,6-dimethylphenyl)-2*H*-benzo[*d*][1,2,3]triazole (**4**)) shifts the reduction potential even more negatively to –2.55 V *vs.* Fc/Fc^{+}. We ascribe the non-linear effect of dimethyl substitution on reduction potential to ground-state conformational effects. Flow battery tests with negolyte **1** and ferrocene posolyte demonstrated >90% Coulombic efficiency at 6.7 mA cm^{-2} with improved cyclability in the presence of lithium bis(trifluoromethylsuylfonyl)imide supporting salt.

Keywords: Nonaqueous Redox Flow Battery, Molecular Modification, Benzotriazole Derivatives, Energy Storage, Dihedral Angle

INTRODUCTION

Efficient and scalable energy storage technologies are paramount in addressing contemporary energy and environmental challenges.[1,2] Redox flow batteries (RFBs) have emerged as key players in the field of stationary energy storage solutions for renewable resources such as wind and solar energy.[3] In RFBs, energy is stored in solutions containing redox-active molecules, which undergo charging and discharging processes as they flow through an electrochemical cell.[4] RFBs are broadly categorized into aqueous and non-aqueous types depending on the solvents used to solubilize the electrolytes. Aqueous RFBs (ARFBs) have made significant strides, with vanadium-based electrolytes achieving successful commercialization.[5] Aqueous electrolytes offer advantages such as non-flammability, high conductivity, and fast electron transfer kinetics.[6] However, ARFBs present low cell potential and, therefore, offer limited energy density, primarily due to the constrained potential window of water.[7] Non-aqueous RFBs (NARFBs), on the other hand, hold promise for achieving high energy density and voltage levels, owing to the expanded potential window offered by non-aqueous electrolytes.[8–10] A critical need in NARFBs is the redox-active molecules as negolyte candidates that can leverage the wide cathodic potential of non-aqueous electrolytes. Our research aims to address the technical and scientific challenges faced by NARFBs, with a particular focus on developing organic molecules that are highly soluble, stable to redox cycling, and display highly negative reduction potential to serve as negolytes.

Recently, there has been a growing interest in using organic-based redox molecules in RFBs due to their tunable structures, sustainability at the elemental level, and cost-effectiveness.[11–13] Incorporating organic molecules into ARFBs has proven successful in enhancing energy density, solubility, and electrochemical stability. Numerous organic molecules, such as 9-fluorenone,[14] 4-methoxyazobenzene,[15] and 5-nitro-1,1,3,3-tetramethylisoindoline-2-yloxyl,[16] have been identified as potential redox species for NARFBs. Despite these efforts, only a handful of negolytes exhibit stable reduction events at potentials more negative than −2.0 V *vs.* ferrocene/ferrocenium (Fc/Fc^+).[17,18] Because the overall cell voltage is determined by the difference in reduction potentials of the cell components, it is important to maximize the potential difference between the negolyte and posolyte redox couples (*i.e.*, more negative reduction potential for the negolyte couple and more positive reduction potential for the posolyte). In general, efforts to maximize the potential difference can encounter limitations regarding the chemical and electrochemical stability of the negolyte and posolyte during charging-discharging cycling. In particular, the stability of most radical anions formed during single-electron reduction is a concern.[19] Other common challenges include the cross-over of active species between the negolyte to posolyte compartments that reduce the storage capacity over repeated charging-discharging cycles,[20] and the necessity of new ion-selective separators based on the new negolyte-posolyte chemistries.[21]

Among the negolytes investigated to date, 2,1,3-benzothiadiazole (BzNSN) (**Scheme 1a** top left structure) stands out for its remarkably negative reduction potential, approaching approximately −1.58 V *vs*. Ag/Ag^+ in a 0.5 M lithium bis(trifluoromethanesulfonyl)imide (LiTFSI)/acetonitrile (ACN) solution.[22] Over the last few years, BzNSN derivatives have been synthesized by introducing various substituents onto the benzene ring, which is the redox-active core.[23,24] These modifications aimed to improve the electrochemical cycling performance and the stability of the radical anion that forms upon reduction (**Scheme 1b**). For instance, introducing a strongly electron-donating methoxy (MeO–) substituent in the arene ring (at carbon-5) resulted in a ∼100 mV more negative reduction potential.[24] In a recent study, Yan *et al.*[25] highlighted the potential use of benzotriazole (BTZ) derivatives as negolytes for NARFBs by replacing sulfur in BzNSN with nitrogen. This substitution strategy aims to enhance the π-electron density on the aromatic core, leading to a more negative reduction potential. The replacement of divalent sulfur with trivalent nitrogen also introduced an exocyclic substituent, providing an additional structural component with which to optimize reduction potential, radical anion stability, and solubility.

We developed a series of new BTZ derivatives (**Scheme 1a**) with the aim of pushing the redox potentials more negative for increased cell potentials and negolyte concentrations and investigated their electrochemical behavior in non-aqueous electrolytes (redox reaction shown in **Scheme 1b**). Our investigations revealed that the inclusion of an *o*-tolyl group on the N2-nitrogen (*i.e.*, compound **1**) resulted in a notably lower reduction potential of –2.25 V *vs.* Ag/Ag$^+$ (–2.35 V *vs.* Fc/Fc$^+$) with enhanced solubility of 3.5 M in *N,N*-dimethylformamide (DMF). The *o*-tolyl substituent resulted in a more negative reduction potential than related *m*-tolyl (**2**, –2.24 V *vs.* Fc/Fc$^+$) and *p*-tolyl (**3**, –2.28 V *vs.* Fc/Fc$^+$) derivatives. Moreover, 2,6-dimethyl substitution (**4**) further reduces the reduction potential to –2.45 V *vs.* Ag/Ag$^+$ (–2.55 V *vs.* Fc/Fc$^+$), underscoring the electrochemical tunability of the BTZ family of negolytes. Density functional theory (DFT) calculations demonstrate a direct correlation between the LUMO energy, which is exquisitely sensitive to ground state conformation, and the reduction potential, as well as between the energy gap of HOMO-LUMO and the rate of electron transfer. A flow cell analysis featuring the ortho-substituted derivative (**1** in **Scheme 1a**) as a negolyte and ferrocene as a posolyte exhibited a cell potential of 2.35 V and a theoretical capacity of 93.8 Ah L^{-1}. A prototype NARFB incorporating the BTZ derivative (**1** in **Scheme 1a**) and ferrocene was evaluated for battery performance, revealing the importance of system-level interactions in dictating cyclability.

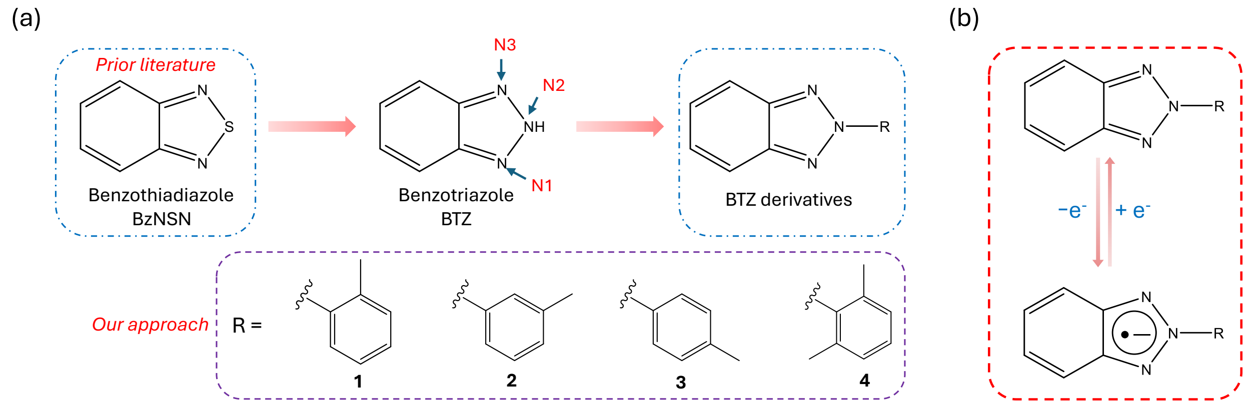

Scheme 1. (a) Molecular structures of BzNSN, BTZ, and BTZ derivatives. The BTZ derivatives were synthesized in this study with R substitution in N2 nitrogen. R = *ortho*-tolyl (**1**), *meta*-tolyl (**2**), *para*-tolyl (**3**), and 2,6-dimethylphenyl (**4**). (b) A general representation of the one-electron redox process in BTZ and BTZ derivatives.

MATERIALS AND METHODS

Materials. All chemicals and solvents were obtained as ACS reagent grade and used as received. Dry toluene and acetonitrile (purchased from Fisher Scientific, HPLC grade) were obtained from a drying column. NMR solvents were purchased from Cambridge Isotope Laboratories and were used as received. All reactions were carried out under an ambient atmosphere unless otherwise noted.

Characterization Details. ^{1}H and ^{13}C NMR spectra were recorded on an Inova 500 FT NMR (Varian), an Acsend^{TM} 400 NMR (Bruker), or an Acsend^{TM} 400 NMR (Bruker) and were referenced against residual proteo solvent signals: $CDCl_3$ (7.26 ppm, ^{1}H; 77.16 ppm, ^{13}C), $(CD_3)_2SO$ (2.50 ppm, ^{1}H), and acetonitrile-d_3 (1.94 ppm, ^{1}H; 1.32 ppm, ^{13}C).[12] ^{1}H NMR data are reported as follows: chemical shift (δ, ppm), (multiplicity: s (singlet), d (doublet), t (triplet), m (multiplet), integration). ^{13}C NMR data are reported as follows: chemical shift (δ, ppm). Mass spectrometry data were recorded on either Orbitrap Fusion$^{\text{TM}}$ Tribrid$^{\text{TM}}$ Mass Spectrometer or Q Exactive$^{\text{TM}}$ Focus Hybrid Quadrupole-Orbitrap$^{\text{TM}}$ Mass Spectrometer from ThermoFisher Scientific.

Electrochemical Measurements. The ionic conductivities of different supporting electrolytes were measured by the electrochemical impedance spectra using two platinum electrodes. The cyclic voltammetry (CV) and rotating disk electrode (RDE) measurements were conducted on the BioLogic electrochemical workstation. Both CV and RDE tests used the three-electrode configuration with glassy carbon as the working electrode (diameter 3 mm for CV and diameter 5 mm for RDE), Ag/AgNO$_3$ (0.01 M) in ACN with 0.1 M TEAP as the reference electrode, and graphite rod as the counter electrode. 5 mM of redox molecules dissolved in acetonitrile (ACN) or *N*,*N*-Dimethylformamide (DMF), using 0.5 M tetraethylammonium tetrafluoroborate (TEABF$_4$) as a support salt. The scan rates in CV tests were 100 mV s^{-1}. In RDE tests, the working current was recorded in the potential range from −1.5 to −2.5 V *vs.* Ag/AgNO$_3$ (0.01 M) at 10 mV s^{-1}. The rotation rates were 100, 225, 400, 625, 900, 1225, 1600, and 2025, r.p.m.

Diffusion Coefficient (*D*). The diffusion coefficient was calculated from the peak intensities of CV curves using the Randles-Sevcik Eq.1:

$$i_p = 2.69 \times 10^5\, n^{3/2} A D^{1/2}\, C^* v^{1/2} \qquad (1)$$

where i_p is the peak current in amperes, n is the number of electrons involved in the half-reaction for the redox couple (1 electron), C* is the initial concentration of active materials in mol cm^{-3} (0.005 M), ν is the scan rate in V s^{-1}, A is electrode area in cm^2 (0.07 cm^2), and *D* is the diffusion coefficient in cm^2 s^{-1}. The CV scan rate varied from 10 to 160 mV s^{-1}, resulting in changes in the intensity of peak currents i_p (peak height in mA). The average peak current was plotted against the square root of different scan rates ($\nu^{1/2}$) to obtain a straight line with a slope. The *D* values were calculated from the slopes of the straight lines.

Rate Constant (*k₀*). The Koutecky–Levich plots at different overpotentials were extrapolated to get the kinetic current i_k according to the Koutecky–Levich Eq. 2:

$$\frac{1}{i}=\frac{1}{i_k}+\frac{1}{0.62nFAD^{2/3}\omega^{1/2}v^{-1/6}C} \tag{2}$$

where n is the number of electrons transferred, F is the Faraday constant (96485 C mol^{-1}), A is the area of the working electrode in cm^2 (0.07 cm^2), *D* is the diffusion coefficient in cm^2 s^{-1}, C is the molar concentration in mol cm^{-3} (0.001 M), ν is the kinetic viscosity in cm^2 s^{-1}, and ω is the routing angular velocity in rad s^{-1}.

The exchange current (i_0) can be obtained by fitting i_k to the Tafel plot at zero overpotential. From which the reaction rate constant (k_0) was determined according to the Butler–Volmer Eq.3.

$$i_0=nFCk_0 \tag{3}$$

Solubility. The solubility of **1** was measured by CV. A calibration curve was made based on five solutions of **1** (at known concentrations of 0.002 M, 0.004 M, 0.006 M, 0.008 M, and 0.01 M) in 0.5 M DMF-$TEABF_4$ or 0.5 M ACN-$TEABF_4$ electrolyte. The cathodic peak current intensity values at a potential of –2.30 V and corresponding concentration values were plotted to obtain a linear correlation equation (Figure S25b and Figure S26b). Subsequently, **1** was added to 100 µL 0.5 M DMF-$TEABF_4$ or 0.5 M ACN-$TEABF_4$ electrolyte solution inside the glovebox until the solids were no longer dissolved. After that, 10 µL of these saturated solutions were each dispensed in a certain amount of 0.5 M DMF-$TEABF_4$ or 0.5 M ACN-$TEABF_4$ electrolyte solution. A CV of this diluted sample was recorded to obtain cathodic peak current intensity. Using the correlation equation, a concentration was determined for this sample, and subsequently, by accounting for dilution, the maximum solubility of **1** in 0.5 M DMF-$TEABF_4$ electrolyte was determined to be 3.5 M and 1.9 M in 0.5 M ACN-$TEABF_4$.

CV Stability Test. A specialized arrangement was devised for conducting calendar life assessments, ensuring a consistent separation between the working and reference electrodes to minimize fluctuations in i_{pa}/i_{pc}. A 20 mL glass vial equipped with Teflon-lined screw caps was utilized. For periodic CV analysis spanning 7 days, the vial lid was replaced with a custom cap featuring three holes precisely designed to snugly accommodate the counter, working, and reference electrodes, securely holding them in position. A Teflon holder was strategically positioned midway along their height to maintain a consistent distance between the working and reference electrodes. Following each CV test, the sample was resealed using the Teflon-lined screw cap.

H-Cell Cycling. Charge/discharge measurements with a custom glass H-cell were carried out in an Ar-filled glovebox using a BioLogic VSP galvanostat. The working and counter electrodes were graphite felts (Morgan Advanced Materials WDF 3 mm); the separator was Daramic 175. An Ag/Ag^+ reference electrode was used on the working side of the H-cell. The electrolyte contained 5 mM active species and 0.50 M $TEABF_4$ in DMF. Both chambers of the H-cell were loaded with 5 mL of the electrolyte solution, and their contents were stirred continuously. For the initial charge, 1 C-rate was applied with a potential cutoff of –2.65 V *vs.* Ag/Ag^+. After the initial charge, the solution on the counter electrode side was exchanged for a fresh solution to enable symmetrical one-electron cycling. The working side was charged at 4 mA (approximately 5 C). Voltage cutoffs were set at 0.3 V higher than $E_{1/2}$ as the upper limit and −0.3 V lower than $E_{1/2}$ as the lower limit.

Flow Cell. Flow cell testing was performed to assess the RFB performance of the developed redox molecule. These experiments were carried out at room temperature in a dry nitrogen glovebox using an in-house built flow cell (PEEK material) with a geometric/ membrane area of 3 cm^2. Experiments were performed at a designated constant current density. The flow cell uses a flow-through carbon felt configuration. The impervious graphite current sheet (Graphite Store) was machined in-house to create the current collectors. A thick graphite felt (Morgan Advanced Materials WDF 3 mm) compressed to 2.5 mm was used as the electrode material. The graphite-felt electrodes were heat-treated at 400 °C for 4 h before use. Daramic 175 (200 μm wetted thickness) was used as a porous separator. The Daramic was soaked in methanol for 24 h to remove residual oil from the manufacturing process and then dried in air before use. Mixed electrolyte featuring a negolyte containing 10 mM of compound **1** and a posolyte containing 15 mM of Fc.

Computational Methods. All computations were carried out using Revision C.01 of the Gaussian 16 suite of programs.[26] To find the lowest energy conformer, a conformational analysis was conducted using the three-parameter Becke model with the Lee−Yang−Par modification B3LYP[27,28] functional in conjunction with the 6-31G+(d,p)[29,30] basis set. The choice of a 1 kcal/mol threshold in the conformational analysis is justified to identify conformations with sufficiently low energy for relevance in the analysis while excluding those with negligible differences. The lowest energy conformers underwent further DFT studies. Geometry optimizations were conducted using the B3LYP functional in conjunction with Grimme's D3 empirical dispersion[31] and Becke-Johnson damping.[32] EMP=D3BJ with the basis set of 6−311G++(d,p).[33] All identified minima were confirmed as stationary points through analytical frequency computations, ensuring there were no imaginary modes.

For finding the rotational barrier transition states, the geometries were optimized using the B3LYP functional with GD3BJ empirical dispersion and an SMD solvation model with parameters equal to DMF as the solvent using the basis set of 6-31G(d').[34] Single points were computed to give more accurate energies at the B3LYP-D3BJ(SMD=DMF)//6-311++(d,p) level of theory on top of the optimized geometry [B3LYP-D3BJ(SMD=DMF)/6-311++(d,p)// B3LYP-D3BJ(SMD=DMF)/6-31G(d')].

UV–Vis absorption spectra were simulated using TD-DFT[35] single points at the B3LYP-D3BJ/6-311++G(d,p)-(SMD-DMF) level of theory on the B3LYP-D3BJ/6-31G(d,p) optimized geometries. The first 30 vertical excitations were solved iteratively. The simulated spectra were generated using a 50 nm broadening on the Gaussian line shape.

All orbital images and optimized structures were visualized using GaussView 6[36] or VMD.[37] NBO calculations on the optimized geometry of the most stable conformers at the same theoretical level were executed using Gaussian. The resulting molecular orbitals were visualized with VMD, employing an isosurface value of 0.019. Dipole moments, expressed in Debye, and NBO charge and NBO spin density were visually represented in GaussView 6, utilizing a fixed color range from -0.5 (red) to +0.5 (green).

RESULTS AND DISCUSSIONS

The BTZ derivatized structures shown in **Scheme 1a** were synthesized by modification of literature methods (see supporting information for details methods).[38] Compounds **1**-**4** are new species and were thus characterized by ^1H and ^{13}C NMR spectroscopy (Figures S1-S13) as well as high-resolution mass spectrometry. The structural assignment of compound **4** was further established by single-crystal X-ray diffraction (Figure S14 and Table S1). The redox chemistry of compounds **1**-**4** was examined by cyclic voltammetry (CV) in both ACN and DMF (Figure S15) with 0.5 M $TEABF_4$. The measured ionic conductivity of the prepared supporting electrolyte with

$TEABF_4$ (Figure S16a) was higher for the ACN-based electrolyte with 0.5 M $TEABF_4$, achieving 36 mS/cm, compared to about 17 mS/cm for DMF-based electrolytes. The measured electrochemical stability windows were over 4 V *vs.* Ag/Ag^+ (Figure S16b and S16c). Three metrics were employed to characterize the electrochemical properties of the BTZ derivatives and identify the optimized electrolyte composition: (i) peak-to-peak separation (ΔE_p), (ii) the ratio of reduction and oxidation peak heights (i_{pc}/i_{pa}), and (iii) the peak current density decay after 500 cycles.

Figure 1a shows the CV of compound **1** (5 mM) in DMF with 0.5 M $TEABF_4$ supporting salt. The observed half-wave reduction potential ($E_{1/2}$) of –2.25 V *vs.* Ag/Ag^+ surpasses that of BzNSN itself (–1.58 V vs. Ag/Ag^+ in 0.5 M LiTFSI-ACN),[22] suggesting that the replacement of sulfur with nitrogen substantially reduces the redox potential. Upon closer examination, the ΔE_p of molecule **1** in DMF was determined as 66 mV, and the i_{pc}/i_{pa} value was 0.99, indicating outstanding electrochemical reversibility in this preliminary assessment. After 500 CV cycles, the redox currents seemed stable, with only minor losses (1.5 %) in the DMF-$TEABF_4$, as seen in **Figure 1a**. In comparison, compounds **2** and **3** exhibited negligible average peak current loss, and **4** displayed 5% loss (Figure S17 and Table S2); the CVs of these compounds are shown in **Figure 2**. Also, compound **1** demonstrated better stability in the DMF-based electrolyte than that of the ACN-based (Figure S18). ACN (pKa = 25) is sufficiently acidic to protonate the BTZ anion radical.[39,40] Consequently, compound **1** is more stable in DMF than in ACN. Upon a prolonged stability test where CVs for 5 cycles were repeated every day for 7 days, compound **1** presented 7% current loss in DMF with 0.5 M $TEABF_4$ as seen in **Figure 1a** (Figure S19 shows the ^{1}H NMR with minor new peaks after CV cycles).

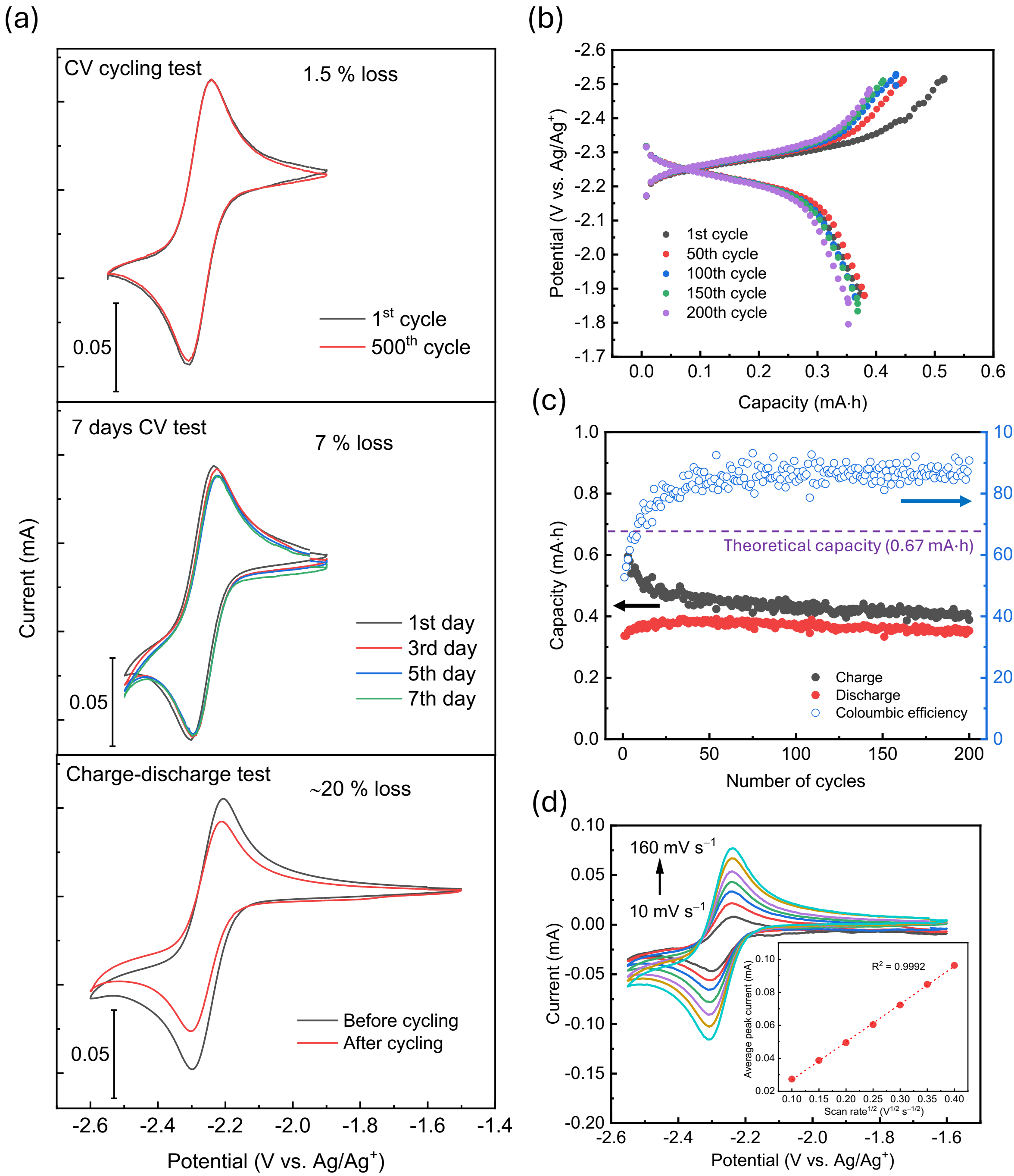

Figure 1. (a) Cycle stability test of **1** (5 mM) in DMF with 0.5 M TEABF$_4$: 500 CV cycles using glassy carbon working electrode at a scan rate of 100 mV s^{-1} (top); 5th CV of the prolonged testing over 7 days (middle); CVs before and after H-cell cycling for 200 charge-discharge cycles (bottom); (b) Charge-discharge curves of **1** (5 mM) measured at 4 mA constant current with

graphite felt electrodes in a symmetrical H-cell; (c) Cycled capacity and measured Coulombic efficiency for **1** in H-cell; (d) CVs of **1** at scan rates of 10-160 mV s^{-1}; inset shows the linear correlation in peak current *vs.* square root of scan rate.

To better examine stability, charge-discharge cycles with 5 mM of compound **1** were performed at 4 mA in a symmetrical H-cell with carbon-felt electrodes. To obtain the reduced form of compound **1** (radical anion in **Scheme 1b**), we initially charged the system at 1 C-rate. The radical anion formation is confirmed by UV-Vis (Figure S20), where both the experimental in-situ UV-Vis measurements and the computed absorption spectrum by time-dependent density functional theory (TD-DFT) show good agreement for excitations of **1** and **1-reduced**. The charge-discharge curves according to the cutoff potentials are shown in **Figure 1b**. The discharge capacity remained consistent at approximately 0.4 mA·h with a Coulombic efficiency greater than 90%, as shown in **Figure 1c.** Because of the applied high current (4 mA; ~ 5 C), material utilization remained at 60%; hence the theoretical capacity was not realized. Post-cycling CV analysis showed no change in the redox potentials; however, when compared to the CV of the as-prepared electrolyte before cycling, there is a 20% current loss as measured at the glassy carbon electrode due to losses at initial charging. In comparison, compound **4** presented a capacity fade of approximately 25% after 200 cycles with a Coulombic efficiency of 80% (Figure S21). Compounds **2** and **3** demonstrate over 90% Coulombic efficiency and maintain stability for 200 cycles with about 10% capacity loss (Figure S22).

The electrokinetics of **1** in DMF were examined through a combination of CV (**Figure 1d**) and rotating disk electrode (RDE) experiments. The diffusion coefficients were estimated based on the CV data utilizing the Randles-Sevcik equation. The obtained diffusivity of 5.90×10^{-6} cm^2

s^{-1} for **1** in DMF-$TEABF_4$ (**Figure 1d**) is an order of magnitude lower than those obtained in ACN (Figure S23), consistent with conductivity trends. However, they remain consistent upon cycling, unlike the case in ACN. Employing the Koutecky–Levich analysis to the RDE data (Figures S24a and S24c) for molecule **1** and analyzing the linear portion of the Tafel plot as a function of overpotentials (Figures S24b and S24d), we calculated the kinetic rate constants (k_0) to be 2.71×10^{-3} cm s^{-1} for DMF-$TEABF_4$ and 6.35×10^{-3} cm s^{-1} for ACN-$TEABF_4$, respectively. The derived diffusion coefficients and rate constants of **1** are comparable to other organic redox active materials employed in non-aqueous systems (Table S3). This underscores the potential applications of **1** in NARFBs.

Since solubility determines the available active concentration in NARFBs and thus the achievable energy densities, we further measured the solubility of **1** in DMF by the concentration-dependent current response in CV.[41] With this method, the saturation concentration was determined to be 3.5 M in DMF (Figure S25). This concentration corresponds to a theoretical capacity of 93.8 Ah L^{-1}. Using the same method, the solubility of **1** in ACN was measured to be 1.9 M (CV in Figure S26), which is lower than in DMF due to the favorable dissolution thermodynamic properties of BTZ derivatives in DMF compared to ACN.[42] Table S4 compares the $E_{1/2}$, solubility, and theoretical volumetric capacity of compound **1** against recently reported benzothiadiazole and benzotriazole derivatives.

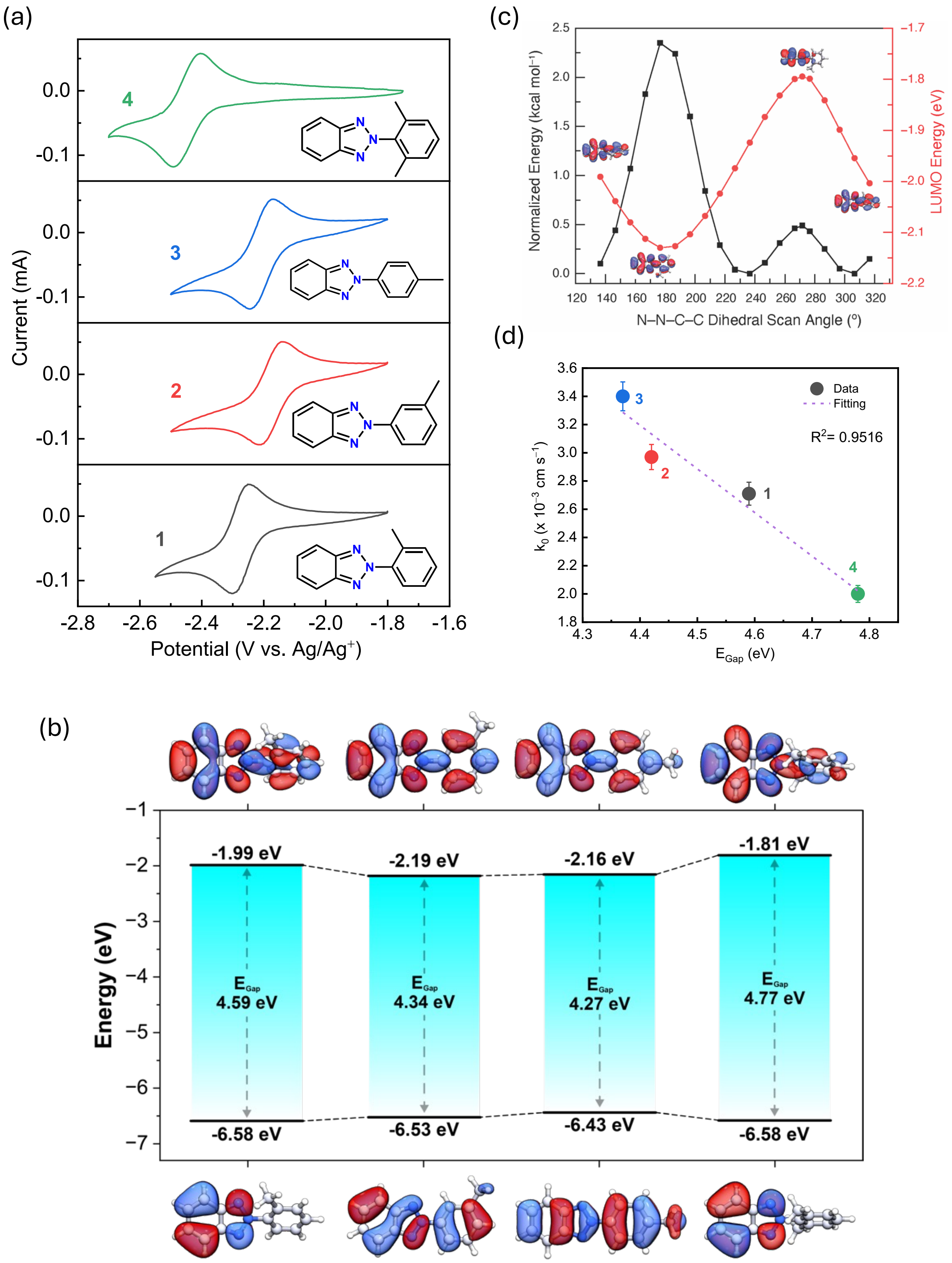
(a)
Current (mA)
0.0
-0.1
4
3
2
1
N
Potential (V vs. Ag/Ag$^+$)
-2.8
-2.6
-2.4
-2.2
-2.0
-1.8
-1.6
(c)
Normalized Energy (kcal mol^{-1})
LUMO Energy (eV)
N–N–C–C Dihedral Scan Angle (°)
120
140
160
180
200
220
240
260
280
300
320
2.5
2.0
1.5
1.0
0.5
0.0
-1.7
-1.8
-1.9
-2.0
-2.1
-2.2
(d)
k_0 (x 10^{-3} cm s^{-1})
E_{Gap} (eV)
Data
Fitting
R^2= 0.9516
3
2
1
4
3.6
3.4
3.2
3.0
2.8
2.6
2.4
2.2
2.0
1.8
4.3
4.4
4.5
4.6
4.7
4.8
(b)
Energy (eV)
-1
-2
-3
-4
-5
-6
-7
-1.99 eV
-2.19 eV
-2.16 eV
-1.81 eV
E_{Gap} 4.59 eV
E_{Gap} 4.34 eV
E_{Gap} 4.27 eV
E_{Gap} 4.77 eV
-6.58 eV
-6.53 eV
-6.43 eV
-6.58 eV

Figure 2. (a) CVs of 5 mM solution of **1**, **2**, and **3** measured in DMF with 0.5 M $TEABF_4$ at a scan rate of 100 mV s^{-1} *vs.* Ag/Ag^+; (b) Calculated HOMO and LUMO energies for **1**, **2**, **3**, and **4** in order from left to right; (c) Normalized electronic energy for the rotation of compound **1** as a function of the N–N–C–C dihedral angle along with the LUMO energies; (d) Plot of experimentally derived electron transfer rate *vs*. HOMO/LUMO energy gap.

While compound **1** demonstrates encouraging reduction potential, solubility, and kinetics for NARFBs, **Figure 2a** demonstrates the further tunable nature of these derivatives. The number and position of the methyl substituents have a significant impact on the reduction potential of the BTZ derivative. While *o*-tolyl derivative **1** displays a more negative reduction potential ($E_{1/2}$ = –2.25 V *vs.* Ag/Ag^+) compared to the isomeric *m*-tolyl ($E_{1/2}$ = –2.14 V *vs*. Ag/Ag^+) (**2,** red) and *p*-tolyl ($E_{1/2}$ = –2.18 V *vs.* Ag/Ag^+) (**3,** blue) analogues, the introduction of methyl substituents at both the 2 and 6 positions (**4**, green) yields the most negative $E_{1/2}$ at –2.45 V *vs.* Ag/Ag^+ as seen in **Figure 2a**.

Of significance, *N*-phenyl substituted BTZ (**7**) in DMF displays a reduction potential of –2.28 *vs.* Fc/Fc^+ (Figure S27). The introduction of a single *ortho*-methyl substituent (compound **1**) moves the reduction potential by 70 mV more negative. Introducing a second *ortho*-methyl substituent (compound **4**) moves the reduction potential by an additional 200 mV, which is far in excess of what one might expect based on simple linear free energy relationships (LFER) based on substituent effects. Furthermore, we have synthesized 2-(2-methoxyphenyl)-2*H*-benzo[*d*][1,2,3]triazole **5** (electron rich N2–aryl; $\sigma = -0.39$, 2-(2-(trifluoromethyl)phenyl)-2*H*-benzo[*d*][1,2,3]triazole **6** (electron deficient N2–aryl; $\sigma = 0.54$), According to literature data,[43] the

Hammett value for *ortho*-substituted aryls for –OMe and –Me (where Me is methyl) are –0.39 and –0.17 respectively. As the Hammett parameter values are additive, the overall Hammett value for compound **4** can be considered to be –0.34, –0.17 for each –Me substituent. Even though simple Hammett analysis suggests the reduction potential of compound **5** should be greater than compound **4**, we observe otherwise. We hypothesized that the observed non-linearity may be due to different conformational preferences of the molecules under investigation. Consistent with simple LFERs, examination of the LUMO energy (Figure S28) for conformations of *N*-phenyl (**7**), *N*-*ortho*-tolyl (**1**), and *N*-2,6-dimethylphenyl-substituted BTZ (**4**) in which the exocyclic substituent is frozen in a co-planar arrangement with respect to the BTZ core reflect linear variation as a function of substitution: The LUMO energy of the frozen co-planar *N*-phenyl derivative is calculated as –2.21 eV; for **1** it is computed to be –2.13 eV and for **4** it is computed to be –2.03 eV. When this series of compounds is allowed to relax to the lowest-energy geometric conformation, significant differences are observed. **Figure 2b** shows the calculated energy gap (E_{Gap}) between the LUMO and HOMO energies for the conformations corresponding to the minimized energies. For **1,** the minimum energy geometry is observed to be skewed with an N–N–C–C dihedral angle of 136°. Rotation of the N–C bond has a free energy rotational of 3.6 kcal mol^{-1}. **Figure 2c** shows the rotational electronic energy along the N–N–C–C dihedral angle starting at the minimum energy geometry (136°) and rotating 180°. Of note, **Figure 2c** plots electronic energy as the structures reflect frozen-coordinate calculations. The rotational barriers are described by Gibbs free energies. There are small numerical differences in these energies but the trends are identical. The coplanar geometry is thus displayed at 180º, and the orthogonal geometry is shown at 270°. The lowest LUMO energy can be seen when the two rings are coplanar with a dihedral angle of ~180°. In contrast, the minimum energy geometry of **4** is mostly orthogonal with a N–N–C–C dihedral angle of 103°; the corresponding free energy barrier to N–C rotation is calculated as 12.3 kcal mol^{-1} (Figure S29). These contrast to the *N*-phenyl derivative, **2,** and **3** where the minimum geometry is the co-planar arrangement. The methyl substituents are so sterically imposing that the highest energy conformation is the co-planar arrangement for both **1** and **4**.

Following a one-electron reduction, significant conformational changes are observed (Figure S30). For **1-reduced**, the lowest energy conformation is the co-planar arrangement. In contrast, the minimum energy of **4-reduced** is still an out-of-plane arrangement but one that is slightly more co-planar than **4** with an N–N–C–C dihedral angle of 131º.

The importance of N–C rotation on the LUMO energy is clear: For **1**, in the minimum energy geometry, the LUMO energy is calculated to be –1.99 eV as in **Figure 2b** (*c.f.* LUMO of co-planar geometry is –2.13 eV and for orthogonal geometry is –1.80 eV as seen in **Figure 2c**). For **4,** in minimum energy geometry (N–N–C–C dihedral angle of 103º), the LUMO energy is calculated to be –1.81 eV as in **Figure 2b** (*c.f.* LUMO of co-planar geometry is –2.03 eV and for orthogonal geometry is –1.79 eV as seen in Figure S30). These contrast with the *N*-phenyl derivative where the minimum energy geometry (completely co-planar) has a LUMO energy of –2.21 eV (*c.f.* LUMO of orthogonal geometry is –1.80 eV as seen in Figure S30). Although the coplanar geometries for compounds **1–4** and the *N*-phenyl derivative have the lowest LUMO energies, minimum electronic energy geometries for both **1** and **4** are not the coplanar geometries. The conformational ground states of **1** and **4** are both significantly twisted out of planarity, which raises the LUMO and thus results in a more negative reduction potential. Given the substantial rotational barrier calculated for **4** as compared to **1** (12.3 *vs.* 3.6 kcal/mol), **4** spends far less time sampling easily reduced geometries than **1**.

The measured redox rate constants (k_0) exhibited a close association with E_{Gap} (**Figure 2c**), where with decreasing E_{Gap}, k_0 increases (see also Table S5). The associated CVs (Figure S31; *D*) and LSVs (Figure S32; k_0) were analyzed in the same manner as explained earlier for compound **1**. In several NARFB studies examining redox-active organic molecules such as methyl viologens[44,45] and quinone derivatives,[46,47] it was found that E_{Gap} is a good indicator for solvent reorganization energy (λ) where a decreasing E_{Gap} correlates with a decreasing λ. Thus, we can further make the inverse correlation between the E_{Gap} and k_0 through the Marcus theory, which states that the electrokinetics increase as the solvent reorganization energy gets smaller. This implies that without significant charge localization, the solvent does not reorganize as substantially to compensate, thus enhancing kinetics. The observed correlation between the measured k_0 and the calculated E_{Gap} is, therefore, reasonable in light of the theory and prior examples.

From the optimized geometries, we also examined the spin density distributions (Figure S33). These analysis suggests that the electrochemical stability of BTZ derivatives hinges primarily on the spin density distribution in the radical anions, particularly at the N2 nitrogen site: higher spin density values correlate with reduced stability. Substituting methyl groups at the ortho (**1**) and meta (**2**) positions yields NBO spin values of 0.09, slightly lower than the para- (**3**) (0.1) and 2,6-dimethyl (**4**) (0.12) counterparts, suggesting that molecule **4** marginally less stable compared to the others (Table S6). This trend is better seen in Figure S34, where the trend in NBO spin densities follows the loss in peak current density upon 500 CV cycles where **1** presents the highest relative stability, and **4** presents the lowest relative stability.

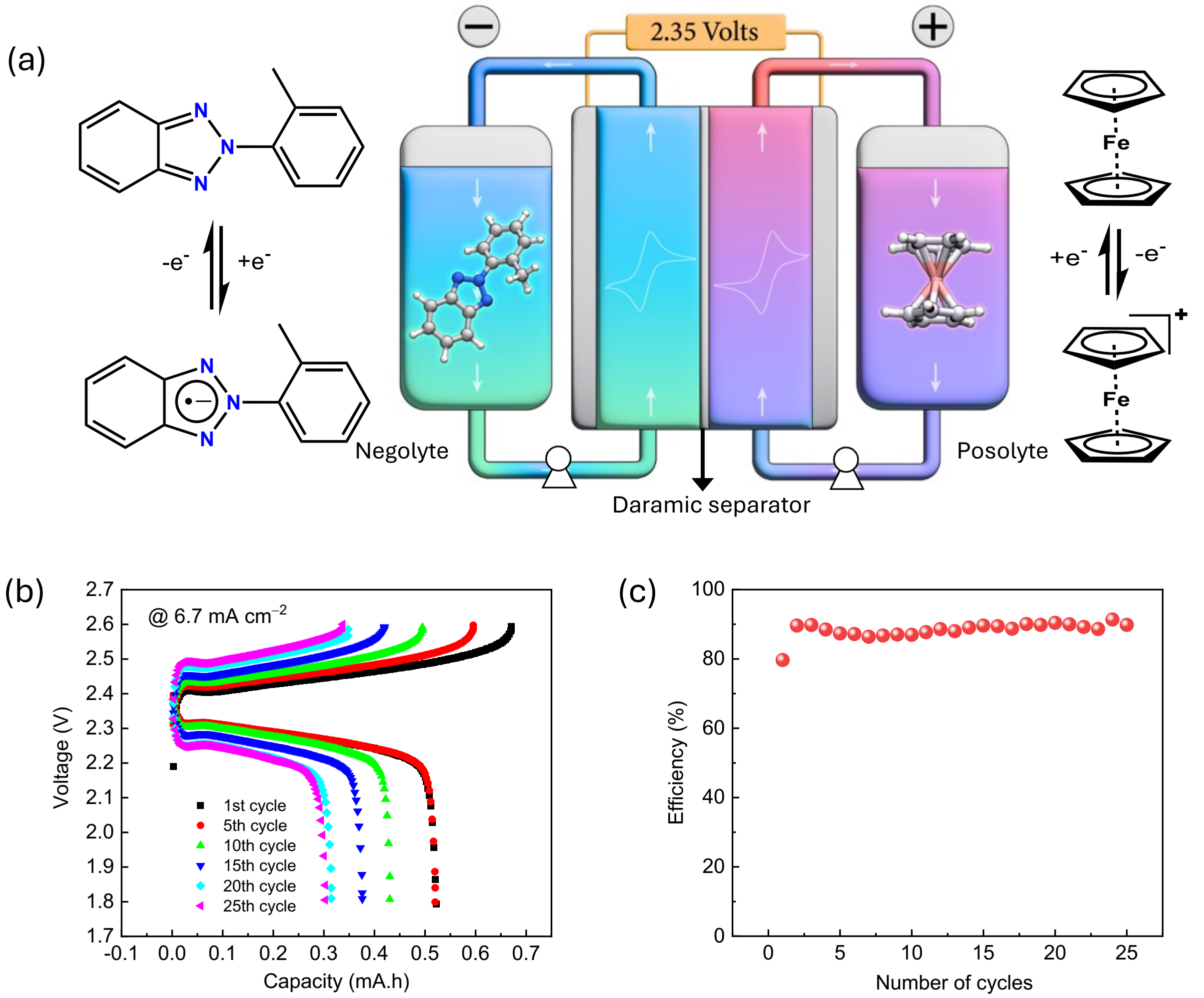

Figure 3. (**a**) Schematic of the **1**/Fc NARFB with structural drawings showing the cell reactions of the **1** negolyte and the Fc posolyte; (**b**) Charge and discharge curves were collected at current densities of 6.7 mA cm^{-2} for the **1**/Fc NARFB; (**c**) Plots of average Coulombic efficiency (CE) for the **1**/Fc NARFB.

In order to further assess the stability at the system level and the potential of the developed compounds for NARFBs, flow battery tests were performed. Using ferrocene as a posolyte with synthesized benzotriazole derivatives, the overall cell potential reached 2.55 V for molecule **4** and 2.35 V for molecule **1** (Figure S35). A specific flow cell configuration was employed[48] to achieve the maximum current density, featuring a negolyte containing 10 mM of compound **1** and a posolyte containing 15 mM of Fc. Graphite felt was the electrode material in the flow cell setup, while a Daramic 175 membrane acted as the separator (**Figure 3a**). Based on the CV analysis, the solvent of choice was DMF. Additionally, $TEABF_4$ and LiTFSI (Lithium bis (trifluoromethane sulfonyl) imide) were utilized as supporting salts in the electrolyte solutions. When 0.5 M DMF-$TEABF_4$ was used as the electrolyte, the NARFB exhibited suboptimal cycling performance even at a low current density of 5 mA cm^{-2} (Figure S36a). A significant drop in discharge capacity, exceeding 50%, was observed after 25 cycles, accompanied by poor Coulombic Efficiency (Figure S36b). This suggests that $TEABF_4$ may not be the most suitable supporting salt for this system.

Stabilizing the anion radical is critical to improving cycling performance. Recently, a lithium-coupled reaction mechanism was proposed in azobenzene redox molecule to improve the cycling performance in NARFBs through the ability of Li^+ to coordinate with the radical anion.[15] Adapting the same approach, 0.5 M LiTFSI in DMF was used as a supporting electrolyte. A substantial improvement in battery performance was achieved; after 25 cycles at a higher current density of 6.7 mA cm^{-2}, the discharge capacity loss remained below 50%, coupled with an impressive CE of over 90% (**Figure 3b** and **3c**). This enhancement is attributed to the stabilization of the anion radical by the Li^+ ion. To gain insights into the redox behavior of the molecules involved, CVs of both the posolyte and negolyte were recorded after the cycling test. As depicted in Figure S37a, alterations in the redox peaks were evident, suggesting changes in the electrochemical behavior of both molecule **1** and Fc. Furthermore, the electrochemical impedance spectroscopy analysis revealed increased charge transfer resistance, ohmic resistance, and mass transfer resistance (Figure S37b). Following the cycling of compound **1**, we analyzed the crude anolyte mixture using ^1H NMR. The resulting spectrum displayed the signals expected for compound **1**, along with a new set of spectral features that we attribute to 2-(o-tolyldiazenyl)aniline

8 (Figure S38). As described by Lund et al.,[49] during the reductive electrolysis of 1-phenyl-1H-benzo[d][1,2,3]triazole in protic media, an azobenzene radical intermediate forms to proceed with the formation of diphenylamine.[49] Based on the literature and the NMR analysis, we suggest a similar and plausible mechanism for the degradation of compound **1** where the triazole ring opening occurs (Figure S39).[49]

CONCLUSION

In summary, a family of benzotriazole derivatives with systematically varied exocyclic *N*-substituents was prepared where the reduction potential was altered towards more negative potentials for higher voltage flow batteries. Compound **1**, featuring an *N*-*o*-tolyl substituent, exhibited a reduction potential of –2.35 V *vs.* Fc/Fc$^+$ and high solubility in DMF. The reduction potential was further decreased to –2.55 V *vs.* Fc/Fc$^+$ by introducing dimethyl substitution (compound **4**). The significant impact of the second methyl substituent (*i.e.* **4** compared with **1**) was attributed to ground state conformational differences and significant impacts on rotational barriers, which demonstrate the importance of stereoelectronic effects of negolytes design. DFT calculations suggest a correlation between the LUMO energy and the reduction potential, as well as between the HOMO-LUMO energy gap and the rate of electron transfer. Flow battery tests with compound **1** as the negolyte and ferrocene as the posolyte demonstrated a cell potential of 2.35 V and a theoretical capacity of 93.8 Ah L^{-1}. Although the cyclability was limited due to possible side reactions at the system level, the NARFB exhibited improved cycling performance with LiTFSI as the supporting electrolyte compared to TEABF$_4$, highlighting the importance of supporting salts in influencing cyclability. In summary, we uncover unexpected non-linear impacts of simple substitution on the reduction potential of triazole based organic negolytes, enabling cell potentials reaching 2.5 V. Computations indicate critical stereoelectronic factors that give rise to the observed enhancements in reduction potential, which suggest conformational strategies as new design elements for flow battery electrolytes.

ASSOCIATED CONTENT

The synthesis procedure of benzotriazole derivatives; crystal structures and NMRs; CVs and LSVs for electrokinetic analysis; H-cell cycling; UV-Vis spectra; additional stability and flow battery tests; molecular coordinates; calculated molecular orbitals and NBO spin densities.

ACKNOWLEDGEMENTS

This study was funded by Breakthrough Electrolytes for Energy Storage Systems (BEES2)—an Energy Frontier Research Center (EFRC) of the U.S. Department of Energy, Office of Science, Basic Energy Sciences under Award # DE-SC0019409. Computational studies by M.T.F. were supported by the Welch Foundation (A-1907).

AUTHOR CONTRIBUTIONS

Palani Sabhapathy – investigation, formal analysis, data curation, writing-original draft, writing-review & editing

Uddalak Sengupta – methodology, data curation, writing-original draft

Miguel Munoz – investigation, visualization

Eda Cagli – conceptualization, methodology

Matthew T. Figgins – data curation, formal analysis

Jesse Wainright – conceptualization, resources, funding acquisition, supervision

David C. Powers – conceptualization, funding acquisition, validation, writing-original draft, writing-review & editing, supervision

Burcu Gurkan – conceptualization, funding acquisition, validation, project administration, writing-original draft, writing-review & editing, supervision

REFERENCES

(1) Dunn, B.; Kamath, H.; Tarascon, J.-M. Electrical Energy Storage for the Grid: A Battery of Choices System Power Ratings, Module Size. *Science* **2011**, *334* (6058), 928–935. https://doi.org/10.1126/science.1212741.

(2) Yang, Z.; Zhang, J.; Kintner-Meyer, M. C. W.; Lu, X.; Choi, D.; Lemmon, J. P.; Liu, J. Electrochemical Energy Storage for Green Grid. *Chem Rev* **2011**, *111* (5), 3577–3613. https://doi.org/10.1021/cr100290v.

(3) Soloveichik, G. L. Flow Batteries: Current Status and Trends. *Chem Rev* **2015**, *115* (20), 11533–11558. https://doi.org/10.1021/cr500720t.

(4) Wang, W.; Luo, Q.; Li, B.; Wei, X.; Li, L.; Yang, Z. Recent Progress in Redox Flow Battery Research and Development. *Adv Funct Mater* **2013**, *23* (8), 970–986. https://doi.org/10.1002/adfm.201200694.

(5) Li, L.; Kim, S.; Wang, W.; Vijayakumar, M.; Nie, Z.; Chen, B.; Zhang, J.; Xia, G.; Hu, J.; Graff, G.; Liu, J.; Yang, Z. A Stable Vanadium Redox-Flow Battery with High Energy Density for Large-Scale Energy Storage. *Adv Energy Mater* **2011**, *1* (3), 394–400. https://doi.org/10.1002/aenm.201100008.

(6) Singh, V.; Kim, S.; Kang, J.; Byon, H. R. Aqueous Organic Redox Flow Batteries. *Nano Res* **2019**, *12* (9), 1988–2001. https://doi.org/10.1007/s12274-019-2355-2.

(7) Gentil, S.; Reynard, D.; Girault, H. H. Aqueous Organic and Redox-Mediated Redox Flow Batteries: A Review. *Curr Opin Electrochem* **2020**, *21*, 7–13. https://doi.org/10.1016/j.coelec.2019.12.006.

(8) Li, M.; Rhodes, Z.; Cabrera-Pardo, J. R.; Minteer, S. D. Recent Advancements in Rational Design of Non-Aqueous Organic Redox Flow Batteries. *Sustain Energy Fuels* **2020**, *4* (9), 4370–4389. https://doi.org/10.1039/d0se00800a.

(9) Tang, L.; Leung, P.; Xu, Q.; Mohamed, M. R.; Dai, S.; Zhu, X.; Flox, C.; Shah, A. A. Future Perspective on Redox Flow Batteries: Aqueous versus Nonaqueous Electrolytes. *Curr Opin Chem Eng* **2022**, *37,* 100833. https://doi.org/10.1016/j.coche.2022.100833.

(10) Gong, K.; Fang, Q.; Gu, S.; Fong, S.; Li, Y.; Yan, Y. Nonaqueous Redox-Flow Batteries: Organic Solvents, Supporting Electrolytes, and Redox Pairs. *Energy Environ Sci* **2015**, *8*, 3515–3530. https://doi.org/10.1039/c5ee02341f.

(11) Luo, J.; Hu, B.; Hu, M.; Zhao, Y.; Liu, T. L. Status and Prospects of Organic Redox Flow Batteries toward Sustainable Energy Storage. *ACS Energy Lett* **2019**, *4* (9), 2220–2240. https://doi.org/10.1021/acsenergylett.9b01332.

(12) Pahari, S. K.; Gokoglan, T. C.; Chaurasia, S.; Bolibok, J. N.; Golen, J. A.; Agar, E.; Cappillino, P. J. Toward High-Performance Nonaqueous Redox Flow Batteries through Electrolyte Design. *ACS Appl Energy Mater* **2023**, *6* (14), 7521–7534. https://doi.org/10.1021/acsaem.3c00910.

(13) Ding, Y.; Zhang, C.; Zhang, L.; Zhou, Y.; Yu, G. Molecular Engineering of Organic Electroactive Materials for Redox Flow Batteries. *Chem Soc Rev* **2018**, *47* (1), 69–103. https://doi.org/10.1039/c7cs00569e.

(14) Wei, X.; Xu, W.; Huang, J.; Zhang, L.; Walter, E.; Lawrence, C.; Vijayakumar, M.; Henderson, W. A.; Liu, T.; Cosimbescu, L.; Li, B.; Sprenkle, V.; Wang, W. Radical Compatibility with Nonaqueous Electrolytes and Its Impact on an All-Organic Redox Flow Battery. *Angewandte Chemie* **2015**, *127* (30), 8808–8811. https://doi.org/10.1002/ange.201501443.

(15) Zhang, L.; Qian, Y.; Feng, R.; Ding, Y.; Zu, X.; Zhang, C.; Guo, X.; Wang, W.; Yu, G. Reversible Redox Chemistry in Azobenzene-Based Organic Molecules for High-Capacity and Long-Life Nonaqueous Redox Flow Batteries. *Nat Commun* **2020**, *11* (1), 3843. https://doi.org/10.1038/s41467-020-17662-y.

(16) Loomans, B. I.; Bottle, S. E.; Blinco, J. P. Bipolar Isoindoline Nitroxide for Nonaqueous Symmetrical Redox Flow Battery. *Batter Supercaps* **2023**, *6* (6), e202200561. https://doi.org/10.1002/batt.202200561.

(17) Griffin, J. D.; Pancoast, A. R.; Sigman, M. S. Interrogation of 2,2′-Bipyrimidines as Low-Potential Two-Electron Electrolytes. *J Am Chem Soc* **2021**, *143* (2), 992–1004. https://doi.org/10.1021/jacs.0c11267.

(18) Wei, X.; Duan, W.; Huang, J.; Zhang, L.; Li, B.; Reed, D.; Xu, W.; Sprenkle, V.; Wang, W. A High-Current, Stable Nonaqueous Organic Redox Flow Battery. *ACS Energy Lett* **2016**, *1* (4), 705–711. https://doi.org/10.1021/acsenergylett.6b00255.

(19) Armstrong, C. G.; Toghill, K. E. Stability of Molecular Radicals in Organic Non-Aqueous Redox Flow Batteries: A Mini Review. *Electrochem commun* **2018**, *91*, 19–24. https://doi.org/10.1016/j.elecom.2018.04.017.

(20) Hu, B.; Hu, M.; Luo, J.; Liu, T. L. A Stable, Low Permeable TEMPO Catholyte for Aqueous Total Organic Redox Flow Batteries. *Adv Energy Mater* **2022**, *12* (8), 2102577. https://doi.org/10.1002/aenm.202102577.

(21) Yuan, J.; Pan, Z. Z.; Jin, Y.; Qiu, Q.; Zhang, C.; Zhao, Y.; Li, Y. Membranes in Non-Aqueous Redox Flow Battery: A Review. *J Power Sources* **2021**, *500*, 229983. https://doi.org/10.1016/j.jpowsour.2021.229983.

(22) Duan, W.; Huang, J.; Kowalski, J. A.; Shkrob, I. A.; Vijayakumar, M.; Walter, E.; Pan, B.; Yang, Z.; Milshtein, J. D.; Li, B.; Liao, C.; Zhang, Z.; Wang, W.; Liu, J.; Moore, J. S.; Brushett, F. R.; Zhang, L.; Wei, X. "Wine-Dark Sea" in an Organic Flow Battery: Storing Negative Charge in 2,1,3-

Benzothiadiazole Radicals Leads to Improved Cyclability. *ACS Energy Lett* **2017**, *2* (5), 1156–1161. https://doi.org/10.1021/acsenergylett.7b00261.

(23) Huang, J.; Duan, W.; Zhang, J.; Shkrob, I. A.; Assary, R. S.; Pan, B.; Liao, C.; Zhang, Z.; Wei, X.; Zhang, L. Substituted Thiadiazoles as Energy-Rich Anolytes for Nonaqueous Redox Flow Cells. *J Mater Chem A* **2018**, *6* (15), 6251–6254. https://doi.org/10.1039/c8ta01059e.

(24) Zhao, Y.; Yu, Z.; Robertson, L. A.; Zhang, J.; Shi, Z.; Bheemireddy, S. R.; Shkrob, I. A.; Y Z; Li, T.; Zhang, Z.; Cheng, L.; Zhang, L. Unexpected Electrochemical Behavior of an Anolyte Redoxmer in Flow Battery Electrolytes: Solvating Cations Help to Fight against the Thermodynamic-Kinetic Dilemma. *J Mater Chem A* **2020**, *8* (27), 13470–13479. https://doi.org/10.1039/d0ta02214d.

(25) Yan, Y.; Zhang, L.; Walser-Kuntz, R.; Vogt, D. B.; Sigman, M. S.; Yu, G.; Sanford, M. S. Benzotriazoles as Low-Potential Anolytes for Non-Aqueous Redox Flow Batteries. *Chem. Mater.* **2022**, *34* (23), 10594–10605. https://doi.org/10.1021/acs.chemmater.2c02682.

(26) Frisch, M. J.; Trucks, G. W.; Schlegel, H. B.; Scuseria, G. E.; Robb, M. A.; Cheeseman, J. R.; Scalmani, G.; Barone, V.; Petersson, G. A.; Nakatsuji, H.; Li, X.; Caricato, M.; Marenich, A. V.; Bloino, J.; Janesko, B. G.; Gomperts, R.; Mennucci, B.; Hratchian, H. P.; Ortiz, J. V.; Izmaylov, A. F.; Sonnenberg, J. L.; Williams-Young, D.; Ding, F.; Lipparini, F.; Egidi, F.; Goings, J.; Peng, B.; Petrone, A.; Henderson, T.; Ranasinghe, D.; Zakrzewski, V. G.; Gao, J.; Rega, N.; Zheng, G.; Liang, W.; Hada, M.; Ehara, M.; Toyota, K.; Fukuda, R.; Hasegawa, J.; Ishida, M.; Nakajima, T.; Honda, Y.; Kitao, O.; Nakai, H.; Vreven, T.; Throssell, K.; Montgomery, J. A.; Jr.; Peralta, J. E.; Ogliaro, F.; Bearpark, M. J.; Heyd, J. J.; Brothers, E. N.; Kudin, K. N.; Staroverov, V. N.; Keith, T. A.; Kobayashi, R.; Normand, J.; Raghavachari, K.; Rendell, A. P.; Burant, J. C.; Iyengar, S. S.; Tomasi, J.; Cossi, M.; Millam, J. M.; Klene, M.; Adamo, C.; Cammi, R.; Ochterski, J. W.; Martin, R. L.; Morokuma, K.; Farkas, O.; Foresman, J. B.; Fox, D. J. Gaussian 16, Rev. C.01. *Gaussian 16, Rev. C. 01* **2016**.

(27) Becke, A. D. Density-functional Thermochemistry. III. The Role of Exact Exchange. *J Chem Phys* **1993**, *98* (7), 5648–5652. https://doi.org/10.1063/1.464913.

(28) Lee, C.; Yang, W.; Parr, R. G. Development of the Colle-Salvetti Correlation-Energy Formula into a Functional of the Electron Density. *Phys Rev B* **1988**, *37* (2), 785–789. https://doi.org/10.1103/PhysRevB.37.785.

(29) Ditchfield, R.; Hehre, W. J.; Pople, J. A. Self-Consistent Molecular-Orbital Methods. IX. An Extended Gaussian-Type Basis for Molecular-Orbital Studies of Organic Molecules. *J Chem Phys* **1971**, *54* (2), 724–728. https://doi.org/10.1063/1.1674902.

(30) Hariharan, P. C.; Pople, J. A. The Influence of Polarization Functions on Molecular Orbital Hydrogenation Energies. *Theoret. chim. Acta* **1973**, *28*, 213–222. https://doi.org/10.1007/BF00533485.

(31) Grimme, S. Semiempirical GGA-Type Density Functional Constructed with a Long-Range Dispersion Correction. *J Comput Chem* **2006**, *27* (15), 1787–1799. https://doi.org/10.1002/jcc.20495.

(32) Grimme, S.; Ehrlich, S.; Goerigk, L. Effect of the Damping Function in Dispersion Corrected Density Functional Theory. *J Comput Chem* **2011**, *32* (7), 1456–1465. https://doi.org/10.1002/jcc.21759.

(33) Krishnan, R.; Binkley, J. S.; Seeger, R.; Pople, J. A. Self-consistent Molecular Orbital Methods. XX. A Basis Set for Correlated Wave Functions. *J Chem Phys* **1980**, *72* (1), 650–654. https://doi.org/10.1063/1.438955.

(34) Petersson, G. A.; Al-Laham, M. A. A Complete Basis Set Model Chemistry. II. Open-shell Systems and the Total Energies of the First-row Atoms. *J Chem Phys* **1991**, *94* (9), 6081–6090. https://doi.org/10.1063/1.460447.

(35) Marques, M. A. L.; Gross, E. K. U. TIME-DEPENDENT DENSITY FUNCTIONAL THEORY. *Annu Rev Phys Chem* **2004**, *55*, 427–455. https://doi.org/10.1146/annurev.physchem.55.091602.094449.

(36) Dennington, R.; Keith, T. A. ;; Millam, J. M. GaussView 6.0. 16. **2016**.

(37) Humphrey, W.; Dalke, A.; Schulten, K. VMD: Visual Molecular Dynamics. *J Mol Graph* **1996**, *14* (1), 33–38. https://doi.org/10.1016/0263-7855(96)00018-5.

(38) Roshandel, S.; Lunn, M. J.; Rasul, G.; Muthiah Ravinson, D. S.; Suri, S. C.; Prakash, G. K. S. Catalyst-Free Regioselective N2 Arylation of 1,2,3-Triazoles Using Diaryl Iodonium Salts. *Org Lett* **2019**, *21* (16), 6255–6258. https://doi.org/10.1021/acs.orglett.9b02140.

(39) Engel, P. S.; Lee, W.-K.; Marschke, G. E.; Shine, H. J. *The Reactions of 1-Adamantyl Radicals with Acetonitrile and Their Bearing on the Oxidative Decomposition of 1,1'-Azoadamantane*; *J. Org. Chem.* **1987**, 52, 2813-2817. https://pubs.acs.org/doi/10.1021/jo00389a031.

(40) Wei, X.; Xu, W.; Huang, J.; Zhang, L.; Walter, E.; Lawrence, C.; Vijayakumar, M.; Henderson, W. A.; Liu, T.; Cosimbescu, L.; Li, B.; Sprenkle, V.; Wang, W. Radical Compatibility with Nonaqueous Electrolytes and Its Impact on an All-Organic Redox Flow Battery. *Angewandte Chemie* **2015**, *127* (30), 8808–8811. https://doi.org/10.1002/ange.201501443.

(41) Al Raihan, M.; Dyker, C. A. Ester-Substituted Bispyridinylidenes: Double Concerted Two-Electron Bipolar Molecules for Symmetric Organic Redox Flow Batteries. *ACS Energy Lett* **2023**, *8* (8), 3314–3322. https://doi.org/10.1021/acsenergylett.3c00969.

(42) Luan, Y.; Li, J.; Kaliwanda, M.; Wang, N.; Chen, K.; Li, X.; Su, W.; Hao, H. Solution Thermodynamics of Benzotriazole in Different Pure Solvents. *J Chem Eng Data* **2018**, *63* (5), 1546–1555. https://doi.org/10.1021/acs.jced.7b01085.

(43) Takahata, Y.; Chong, D. P. Estimation of Hammett Sigma Constants of Substituted Benzenes through Accurate Density-Functional Calculation of Core-Electron Binding Energy Shifts. In *International Journal of Quantum Chemistry*, **2005**, 103, 509–515. https://doi.org/10.1002/qua.20533.

(44) Liu, Y.; Li, Y.; Zuo, P.; Chen, Q.; Tang, G.; Sun, P.; Yang, Z.; Xu, T. Screening Viologen Derivatives for Neutral Aqueous Organic Redox Flow Batteries. *ChemSusChem* **2020**, *13* (9), 2245–2249. https://doi.org/10.1002/cssc.202000381.

(45) Tang, G.; Liu, Y.; Li, Y.; Peng, K.; Zuo, P.; Yang, Z.; Xu, T. Designing Robust Two-Electron Storage Extended Bipyridinium Anolytes for PH-Neutral Aqueous Organic Redox Flow Batteries. *JACS Au* **2022**, *2* (5), 1214–1222. https://doi.org/10.1021/jacsau.2c00184.

(46) Ding, Y.; Li, Y.; Yu, G. Exploring Bio-Inspired Quinone-Based Organic Redox Flow Batteries: A Combined Experimental and Computational Study. *Chem* **2016**, *1* (5), 790–801. https://doi.org/10.1016/j.chempr.2016.09.004.

(47) Sun, P.; Liu, Y.; Li, Y.; Shehzad, M. A.; Liu, Y.; Zuo, P.; Chen, Q.; Yang, Z.; Xu, T. 110th Anniversary: Unleashing the Full Potential of Quinones for High Performance Aqueous Organic Flow Battery. *Ind Eng Chem Res* **2019**, *58* (10), 3994–3999. https://doi.org/10.1021/acs.iecr.8b06391.

(48) Ke, X.; Prahl, J. M.; Alexander, J. I. D.; Savinell, R. F. Mathematical Modeling of Electrolyte Flow in a Segment of Flow Channel over Porous Electrode Layered System in Vanadium Flow Battery with Flow Field Design. *Electrochim Acta* **2017**, *223*, 124–134. https://doi.org/10.1016/j.electacta.2016.12.017.

(49) Pedersen, S. U.; Lund, H. Electrochemical Reduction of Some Benzotriazoles in Protic and Aprotic Media. *Acta Chem Scand* **1988**, *42b*, 319–323. https://doi.org/10.3891/acta.chem.scand.42b-0319.

TOC

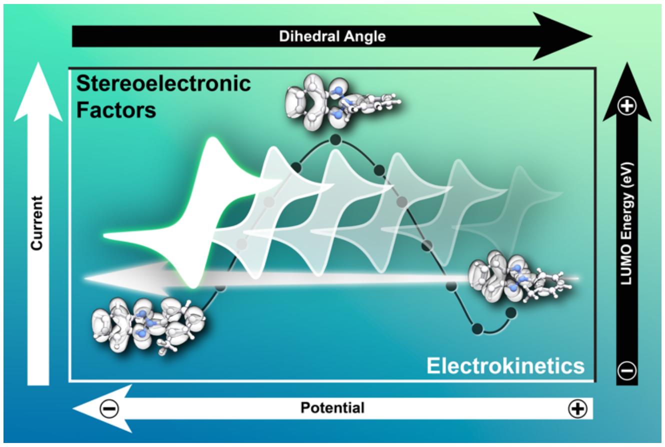
Dihedral Angle
Stereoelectronic Factors
Current
LUMO Energy (eV)
⊕
⊖
Electrokinetics
Potential
⊖
⊕